



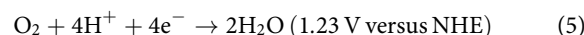
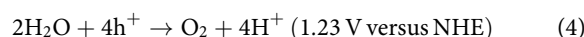
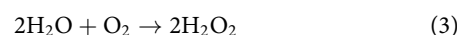
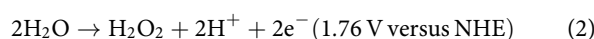
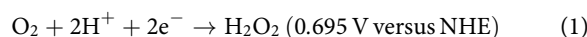
Atomically dispersed antimony on carbon nitride for the artificial photosynthesis of hydrogen peroxide

Zhenyuan Teng^{1,2,8}, Qitao Zhang^{3,8}, Hongbin Yang^{4,8}, Kosaku Kato⁵, Wenjuan Yang³, Ying-Rui Lu⁶, Sixiao Liu^{2,7}, Chengyin Wang⁵, Akira Yamakata⁵, Chenliang Su³, Bin Liu⁴ and Teruhisa Ohno^{1,2}

Artificial photosynthesis offers a promising strategy to produce hydrogen peroxide (H₂O₂)—an environmentally friendly oxidant and a clean fuel. However, the low activity and selectivity of the two-electron oxygen reduction reaction (ORR) in the photocatalytic process greatly restricts the H₂O₂ production efficiency. Here we show a robust antimony single-atom photocatalyst (Sb-SAPC, single Sb atoms dispersed on carbon nitride) for the synthesis of H₂O₂ in a simple water and oxygen mixture under visible light irradiation. An apparent quantum yield of 17.6% at 420 nm together with a solar-to-chemical conversion efficiency of 0.61% for H₂O₂ synthesis was achieved. On the basis of time-dependent density function theory calculations, isotopic experiments and advanced spectroscopic characterizations, the photocatalytic performance is ascribed to the notably promoted two-electron ORR by forming μ -peroxide at the Sb sites and highly concentrated holes at the neighbouring N atoms. The in situ generated O₂ via water oxidation is rapidly consumed by ORR, leading to boosted overall reaction kinetics.

Hydrogen peroxide (H₂O₂) is an important green oxidant¹ widely used in a variety of industries and a promising clean fuel for jet car and rockets^{2–7} (60 wt% H₂O₂ has an energy density of 3.0 mega joules (MJ) l⁻¹, higher than compressed H₂ gas at 35 MPa, 2.8 MJ l⁻¹). Currently, H₂O₂ is manufactured by the energy-consuming, waste-intensive and indirect anthraquinone method^{8,9}. Photocatalytic H₂O₂ synthesis on semiconductor materials from water and oxygen has emerged as a safe, environmentally friendly and energy-saving process^{10,11}. To achieve high efficiency for H₂O₂ production, it is crucial to boost the 2e⁻ oxygen reduction reaction (ORR) (equation (1))¹² or the 2e⁻ water oxidation reaction (WOR) (equation (2))¹³. The light-driven 2e⁻ WOR pathway is not easy to achieve due to the uphill thermodynamics (1.76 V versus normalized hydrogen electrode, NHE); that is, the as-synthesized H₂O₂ will decompose at this highly oxidative potential since H₂O₂ is an excellent hole scavenger^{11,14,15}. On the contrary, the 2e⁻ ORR pathway has been realized for artificial photosynthesis of H₂O₂ in several particulate systems^{12,16–23}. However, the highest apparent quantum yield (ΦAQY) for non-sacrificial H₂O₂ production (equation (3)) is still smaller than 8% (at λ = 420 nm)^{16–24}, much lower than the highest ΦAQY values reached for overall water splitting (roughly 30% at λ = 420 nm)²⁵. To boost the photocatalytic activity for the non-sacrificial H₂O₂ production, both 2e⁻ ORR (equation (2)) and 4e⁻ WOR (equation (4)) should be promoted simultaneously. Unlike some other photocatalytic processes (for example, overall water splitting and N₂ fixation)^{25,26}, these redox reactions cannot be separately considered as irrelevant half reactions, since

O₂ is not only a product in the 4e⁻ WOR (equation (4)), but also a reactant in the 2e⁻ ORR (equation (1)). If the in situ generated O₂ from WOR (equation (4)) can be consumed rapidly by ORR, it will kinetically facilitate the WOR. Therefore, introducing highly active and selective sites for the 2e⁻ ORR in the photocatalytic system to consume the O₂ generated from the WOR offers a promising strategy for breaking the bottleneck of photocatalytic H₂O₂ synthesis.



Manipulating metallic sites can change both the activity and selectivity of ORR²⁷. The O₂ molecular adsorption on metal surface can be generally classified into three types (Fig. 1a): Pauling-type (end-on), Griffiths-type (side-on) and Yeager-type (side-on)^{27,28}. The end-on O₂ adsorption configuration is able to minimize O–O

¹Department of Applied Chemistry, Faculty of Engineering, Kyushu Institute of Technology, Kitakyushu, Japan. ²Joint Laboratory of Yangzhou University, Kyushu Institute of Technology, Yangzhou University, Yangzhou, China. ³International Collaborative Laboratory of 2D Materials for Optoelectronics Science and Technology of Ministry of Education, Institute of Microscale Optoelectronics, Shenzhen University, Shenzhen, China. ⁴School of Chemical and Biomedical Engineering, Nanyang Technological University, Singapore, Singapore. ⁵Graduate School of Engineering, Toyota Technological Institute, Tempaku Nagoya, Japan. ⁶National Synchrotron Radiation Research Center, Hsinchu, Taiwan. ⁷College of Chemistry and Chemical Engineering, Yangzhou University, Yangzhou, China. ⁸These authors contributed equally: Zhenyuan Teng, Qitao Zhang, Hongbin Yang. ✉e-mail: chmsuc@nus.edu.sg; liubin@ntu.edu.sg; tohno@che.kyutech.ac.jp

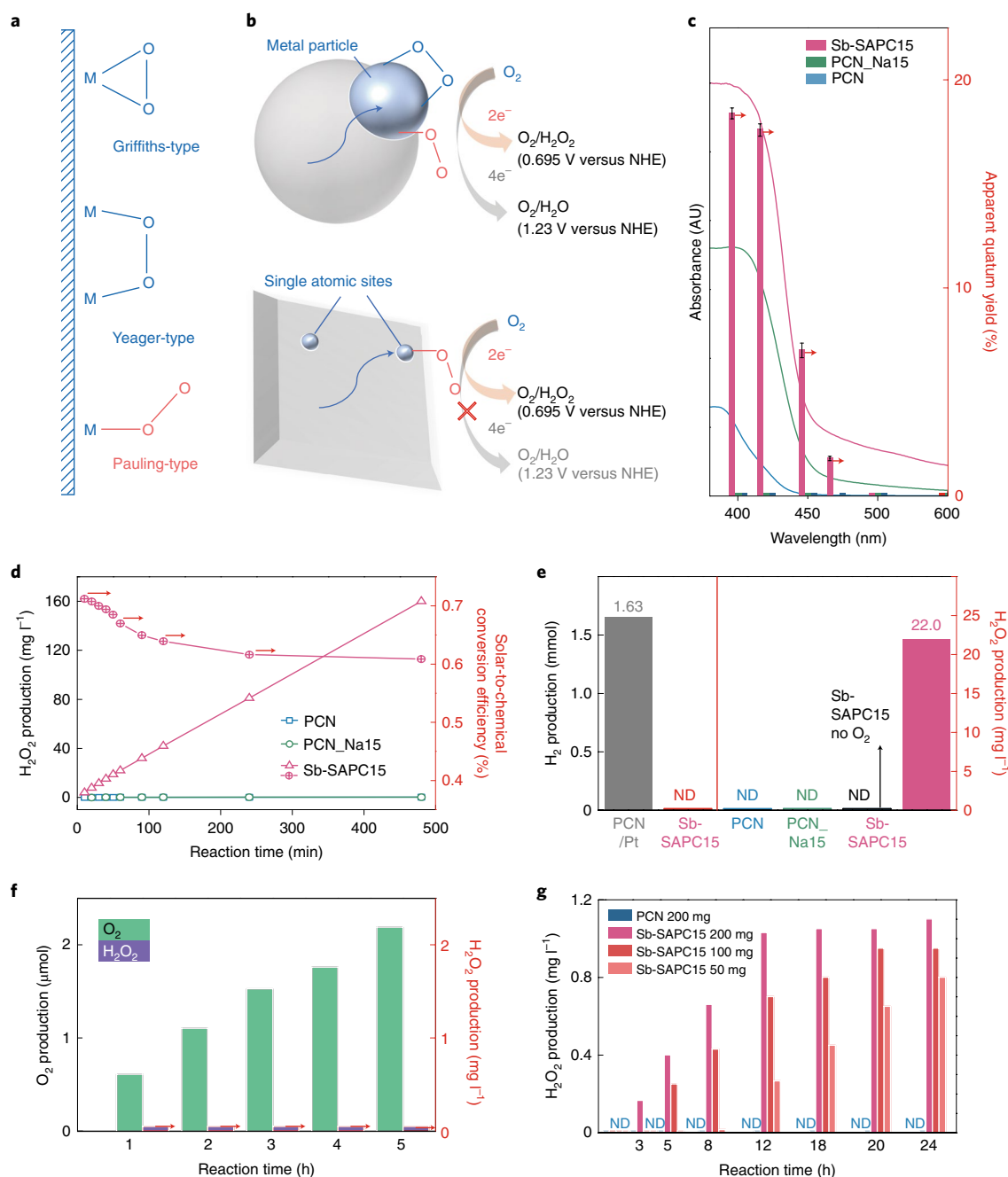


Fig. 1 | Photocatalytic performance of Sb-SAPC towards H_2O_2 production. **a**, Schematic structures of O_2 adsorption on metal surface. **b**, ORR on a metal particle (top) and an isolated atomic site (bottom). **c**, Action spectra of PCN, PCN_Na15 and Sb-SAPC15 towards H_2O_2 production in a phosphate buffer solution (pH = 7.4). Error bars represent the standard deviations of three replicate measurements. **d**, Solar-to-chemical conversion efficiency of PCN, PCN_Na15 and Sb-SAPC15 under AM 1.5 illumination in a phosphate buffer solution. **e**, Selectivity comparison of Sb-SAPC15 and pristine PCN for different photoreduction reactions (reaction time 1 h). Left, comparison of hydrogen evolution activity of Sb-SAPC15 and PCN loaded with 1 wt% Pt in a 10% (v/v) 2-propanol aqueous solution. Right, comparison of activity for photocatalytic H_2O_2 production on pristine PCN, PCN_Na15 and Sb-SAPC15 in a phosphate buffer solution with or without O_2 . **f**, Amount of O_2 and H_2O_2 produced on Sb-SAPC15 in NaO_3 (0.1 M, as the electron acceptor) solution. **g**, Photocatalytic H_2O_2 production with electron acceptor (0.1 mM Ag^+) under N_2 atmosphere. Irradiation conditions were $\lambda > 420$ nm (Xe lamp, light intensity at 420–500 nm, 30.3 W m^{-2}) at 298 K. ND (not detected) in Fig. 1e,g means that H_2O_2 cannot be detected in the photocatalytic system.

bond breaking, leading to the suppression of $4e^-$ ORR (equation (5)) and thus, a highly selective $2e^-$ ORR. On metal particles, both end-on and side-on O_2 molecular adsorption exist, and thus O–O bond splitting on the metal particles' surfaces is difficult to prevent^{29,30}. Benefiting from the desirable features of the single atom catalyst (SAC), the adsorption of O_2 molecules on atomically isolated sites is usually the end-on type, and could therefore reduce the

possibility of O–O bond breaking (Fig. 1b)^{31–34}. For instance, SACs with Pt^{2+} (ref. 35) and Co-N_4 (refs. 36,37) centres could electrochemically reduce O_2 to H_2O_2 via a $2e^-$ ORR pathway with ultrahigh selectivity (>96%). However, Pt^{2+} and Co-N_4 sites are difficult to couple in the photocatalytic system due to their high charge recombination characteristics, which originate from the intermediate band formed by the half-filled *d* electrons. Constructing photocatalysts with

atomically dispersed elements possessing the d^{10} electronic configuration can eliminate the formation of the intermediate band in the band structure, which is favourable for efficient charge separation and formation of reactive centres with a high density of electrons/holes^{15,38,39}. This suggests that SACs with the d^{10} electronic configuration would be ideal candidates for photocatalytic H_2O_2 synthesis via the $2e^-$ ORR.

Herein, we develop a Sb single atom photocatalyst (Sb-SAPC) for non-sacrificial photocatalytic H_2O_2 synthesis in a water and oxygen mixture under visible light irradiation, in which the oxidation state of Sb is regulated to +3 with a $4d^{10}5s^2$ electron configuration. Notably, an apparent quantum efficiency of 17.6% at 420 nm and a solar-to-chemical conversion efficiency of 0.61% are achieved on the as-developed photocatalyst. Combining experimental and theoretical investigations, it is found that the adsorption of O_2 on isolated Sb atomic sites is end-on type, which promotes formation of Sb- μ -peroxide (Sb-OOH), leading to an efficient $2e^-$ ORR pathway for H_2O_2 production. More importantly, the Sb sites also induce highly concentrated holes at the neighbouring melem units, promoting the $4e^-$ WOR. The concept of using SAC to simultaneously boost reduction and oxidation reactions shall provide a design guide to develop more advanced photocatalytic systems for extensive applications.

Results

Photocatalytic H_2O_2 production on Sb-SAPC. The Sb-SAPC was prepared by a wet chemical method using NaSbF_6 and melamine as the precursor (Supplementary Fig. 1). Control samples including pristine polymeric carbon nitride (PCN) and Na^+ incorporated PCNs, were also prepared as references. According to the amount of metal salt added ($x=0.5, 1, 3, 5, 10, 15$ or 20 mmol of NaF or NaSbF_6) into 4 g of melamine, the samples are denoted as PCN_Nax or Sb-SAPCx, respectively. The as-prepared Sb-SAPC reached a quantity of 100 g in one batch, which is very promising for scalable production (Supplementary Fig. 2).

The photocatalytic performance of Sb-SAPC for H_2O_2 production was assessed in a water and oxygen mixture without presence of any sacrificial agents under visible light illumination. As shown in Supplementary Fig. 3, Sb-SAPC15 shows the highest H_2O_2 production rate (12.4 mg l^{-1} in 120 min) among the samples, which is about 248 times higher than pristine PCN (0.05 mg l^{-1} in 120 min). The surface area of Sb-SAPC15 ($1.89 \text{ m}^2 \text{ g}^{-1}$, Supplementary Fig. 4) is only about 1/7.78 of pristine PCN ($14.7 \text{ m}^2 \text{ g}^{-1}$), indicating that the activity per area enhancement induced by introducing Sb into PCN is increased by more than 1,900-fold as compared to pristine PCN. After we optimized the reaction conditions (Supplementary Figs. 5 and 6)¹⁹, the action spectra (Fig. 1c) for H_2O_2 production were measured. The ΦAQY of Sb-SAPC15 at 420 nm was determined to be 17.6%, which is twice of the most efficient photocatalyst (RF-resin, Supplementary Table 1) for non-sacrificial H_2O_2 production¹⁶. The solar-to-chemical conversion efficiency of Sb-SAPC15 reached as high as 0.61% (Fig. 1d), comparable with the most efficient water splitting photocatalyst (roughly 0.8%)²⁵. The Sb-SAPC15 displayed negligible photocatalytic activity for the hydrogen evolution reaction (Fig. 1e). Furthermore, by comparing the photocatalytic products at two different reaction conditions (with and without O_2), the H_2O_2 is clearly produced via the $2e^-$ ORR (no H_2O_2 was detected in the photocatalytic system without O_2 , Fig. 1e). Besides activity, more than 95% of the initial activity (Sb-SAPC15) could be maintained after five consecutive photocatalytic runs indicating good stability (Supplementary Fig. 7a). Reproducibilities of Sb-SAPC15 (five different batches) were also excellent for AQY and solar-to-chemical conversion measurements (Supplementary Fig. 7b,c). The long-term stability and potential for scalable photocatalytic H_2O_2 production using the Sb-SAPC photocatalyst were demonstrated in a fixed bed reactor (Supplementary Fig. 8).

To study the overall reaction for photocatalytic H_2O_2 production, the half redox reactions on Sb-SAPC15 were separately investigated as follows: Sb-SAPC15 in a 2-propanol aqueous solution (2-propanol as an electron donor, 10% v/v) with saturated O_2 (Supplementary Fig. 9) and in a NaIO_3 aqueous solution (NaIO_3 as an electron acceptor) with N_2 (Fig. 1f and Supplementary Fig. 10), respectively, under visible light irradiation, which confirm that the H_2O_2 is indeed produced via the ORR on Sb-SAPC15. Isotope experiments¹⁶ (Supplementary Fig. 11) were further performed to verify the $4e^-$ WOR mechanism, in which Sb-SAPC15 in H_2^{16}O and $^{18}\text{O}_2$ gas was irradiated for 6, 24 and 72 h. Fe^{3+} and high concentration H^+ were added into the reaction system to decompose H_2O_2 to release O_2 , and the evolved gas was analysed by gas chromatography–mass spectrometry. The gaseous product obtained after 6 h reaction exhibited a strong $^{18}\text{O}_2$ (m/z) peak (94.5%) and a weak $^{16}\text{O}_2$ (m/z) peak (25.2%), showing that $\text{H}_2^{18}\text{O}_2$ was produced by O_2 reduction at the initial stage of the reaction. The gaseous product obtained with the increasing reaction time showed a decreased intensity of the $^{18}\text{O}_2$ peak (24 h 55.7%; 72 h 45.5%) and an increased intensity of the $^{16}\text{O}_2$ peak (24 h 32.5%; 72 h 45.5%), indicating that the oxygen generated by WOR gradually participated in the ORR process¹⁶.

To quantitatively reveal the relationship between the WOR and ORR, a low-concentration electron acceptor (0.1 mM Ag^+) was added into the PCN and Sb-SAPC system in the absence of O_2 . In this case, H_2O_2 can only be produced via the reduction of O_2 generated from water oxidation. PCN showed no photocatalytic activity in this condition, while Sb-SAPC gradually produced H_2O_2 in a certain time interval. After that, the H_2O_2 concentration stayed constant at roughly 1.0 mg l^{-1} no matter how much catalyst was used (Fig. 1g). The quantitative relationship between the amount of added Ag^+ and H_2O_2 produced from WOR is discussed in Supplementary Note 1. An isotope experiment using H_2^{18}O was also conducted to confirm that the H_2O_2 generated in the system was indeed derived from the O_2 produced by the $4e^-$ WOR process (Supplementary Fig. 12). The intensity of the $^{18}\text{O}_2$ peak ($m/z=36$) gradually increased with increasing reaction time, indicating that $\text{H}_2^{18}\text{O}_2$ originated from the $^{18}\text{O}_2$ generated by WOR. Therefore, the O_2 generated from WOR in the Sb-SAPC system was rapidly consumed by the $2e^-$ ORR process to produce H_2O_2 .

Characterization of Sb-SAPC. To understand the superb photocatalytic performance of Sb-SAPC for H_2O_2 production, the catalyst synthesis process (Supplementary Figs. 13–17 and Supplementary Note 2) and the structural characteristics of the as-synthesized catalysts were carefully investigated. As revealed in the ζ -potential measurements, negative surface charges appeared on the as-prepared Sb-SAPCs to neutralize the positive charges induced by the incorporated Na and Sb cations (Supplementary Fig. 18). The crystalline structures of Sb-SAPCx show no obvious changes compared to the pristine PCN, as evidenced in the X-ray diffraction patterns and high-resolution transmission electron microscopy (HRTEM) images (Supplementary Note 3 and Supplementary Figs. 19 and 20). As a powerful tool for visualizing individual heavy atoms, high-angle annular dark-field–scanning transmission electron microscopy (HAADF–STEM) was used to further examine the morphology and elemental distribution. The Sb-SAPC15 is composed of aggregated two-dimensional nanosheets, on which Sb and Na elements are homogeneously distributed (Supplementary Fig. 21). For Sb-SAPC0.5, 1, 3, 5, 10 and 15, Supplementary Fig. 22 and Fig. 2a show that the bright spots with high density were uniformly dispersed over the entire carbon nitride matrix. Electron energy loss spectroscopy (EELS) (Fig. 2b and Supplementary Fig. 23) measurement revealed the bright spots corresponding to Sb atoms. The size distribution as displayed in Fig. 2a shows that 99.6% of Sb species are less than 0.2 nm, demonstrating that Sb exists exclusively as isolated single atoms⁴⁰. The mass ratio of Sb species in Sb-SAPC15

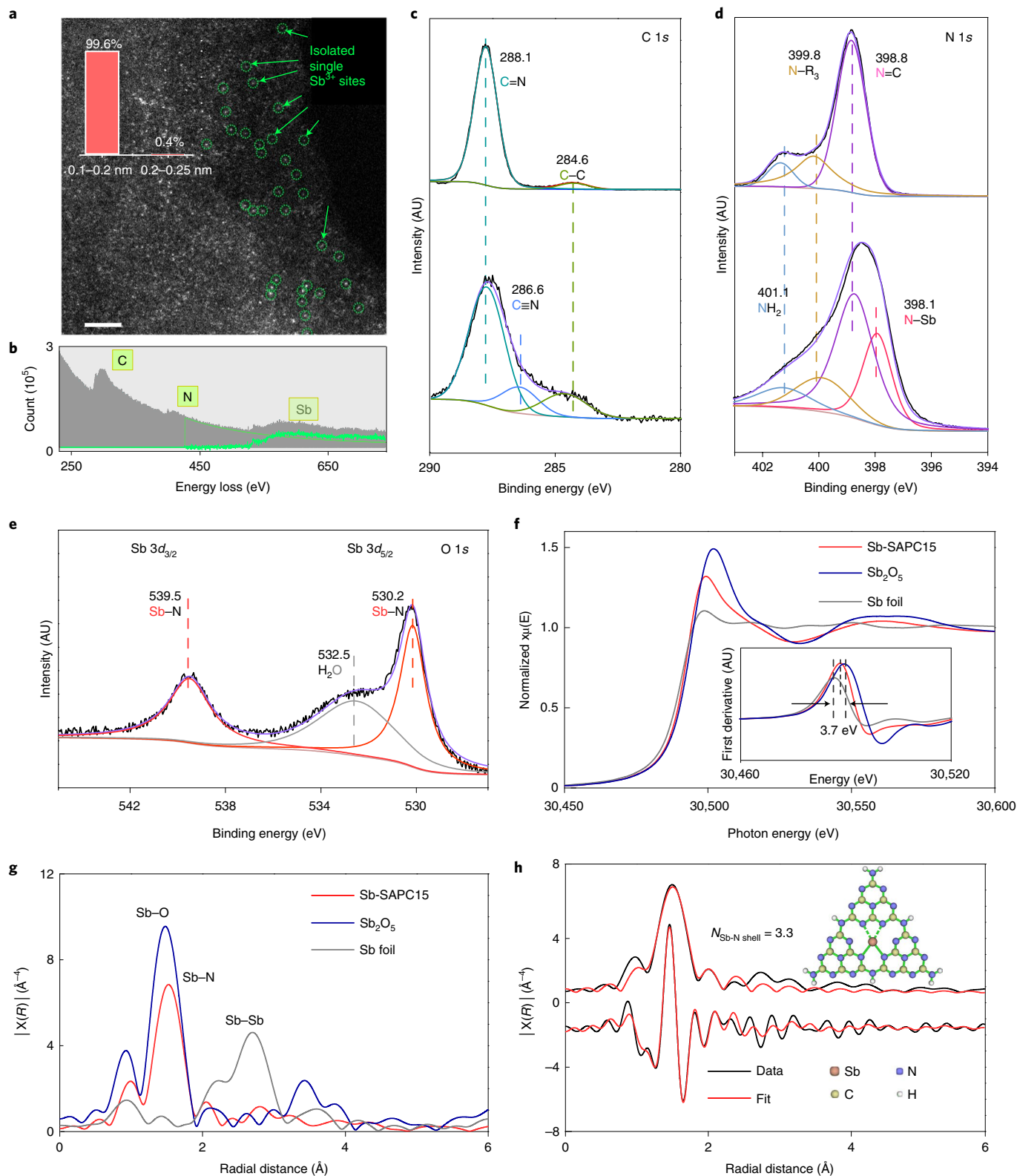


Fig. 2 | Characterization of Sb-SAPC. **a**, High-magnification HAADF-STEM image of Sb-SAPC15. The inset is the size distribution of the bright spots. Scale bar, 2 nm. **b**, EELS spectrum of Sb-SAPC15. **c–e**, High-resolution C 1s (**c**) and N 1s XPS spectra (**d**) of PCN (up) and Sb-SAPC15 (down) and Sb 3d XPS spectrum (**e**) of Sb-SAPC15. **f,g**, Sb K-edge X-ray absorption near edge structure (**f**) and Fourier transform-EXAFS spectra (**g**) of the Sb foil, Sb₂O₅ and Sb-SAPC15. **h**, Fitting of the EXAFS data of the Sb-SAPC15 based on the model obtained from DFT optimization. The insets show optimized molecular models based on DFT for EXAFS fitting. *R* indicates the radial distance in Å.

(10.9 wt%, Supplementary Table 2) is considerably larger than that of the noble or transition metal single atom species in many reported SACs.

To investigate the interaction between the isolated Sb atoms and the PCN skeleton, Fourier transform-infrared and X-ray photoelectron spectroscopy (XPS) measurements were conducted.

The spectra of PCN, PCN_Na15 and Sb-SAPC15 show no obvious difference in the wavenumber ranges of 700–900 and 1,200–1,600 cm^{-1} (Supplementary Fig. 24), indicating that the skeleton of PCN hardly changed before and after incorporation of Na and Sb ions (Supplementary Table 3 and Supplementary Note 4). All fluoride elements have been removed during the calcination process (Supplementary Figs. 25 and 26). In the high-resolution C 1s spectrum of pristine PCN (Fig. 2c), the typical components at around 287.6 and 284.6 eV can be indexed as the C=N and adventitious carbon, respectively. It is important to note that a new nitrogen peak (N 1s) emerges at 398.1 eV in the spectrum of Sb-SAPC15 (Fig. 2d), which can be assigned to the chemical bond of Sb-N. The binding energy of Sb 3d for Sb-SAPC15 (Sb 3d_{3/2} at 539.5 eV and Sb 3d_{5/2} at 530.2 eV) is close to that for Sb₂O₃ (Sb 3d_{3/2} at 539.8 eV and Sb 3d_{5/2} at 530.5 eV)⁴¹, indicating that the oxidation state of Sb in Sb-SAPC15 is close to +3 (Fig. 2e).

The oxidation state of the Sb atoms in Sb-SAPC15 was further determined by the position of the absorption edge in the Sb K-edge X-ray absorption near edge structure (Fig. 2f). The absorption edge for Sb-SAPC15 is 2.2 eV higher than that for the Sb⁰ foil, and 1.5 eV lower than that for Sb⁺⁵₂O₃, suggesting a valence state of around +3 for the Sb atoms in Sb-SAPC15. A Fourier transform-extended X-ray absorption fine structure (FT-EXAFS) spectrum (Fig. 2g) obtained from *k*³-weighted *k*-space (Supplementary Fig. 27) of Sb-SAPC15 shows only one peak at about 1.53 Å, and no Sb–Sb bond at 2.71 Å can be detected, indicating that the Sb sites in Sb-SAPC15 are atomically dispersed. The coordination structure of the Sb atoms was estimated by fitting the EXAFS spectrum of Sb-SAPC15 using Artemis (v.0.9.25)⁴² (Fig. 2h and Supplementary Table 4) based on the density functional theory (DFT) optimization result from the carbon nitride cluster with single Sb sites (Melem_3Sb3⁺, Supplementary Fig. 28c). The best fitting result for the first shell shows that each Sb atom is coordinated with 3.3N atoms on average and can be fitted well with the optimized DFT model (Supplementary Fig. 28d), further indicating that the Sb species are atomically dispersed, consistent with the HAADF-STEM results (Fig. 2a and Supplementary Fig. 22). It is noteworthy that postcharacterizations of Sb-SAPC15 after continuous reaction for 5 days are almost the same as the fresh ones (Supplementary Fig. 29), confirming the excellent stability of Sb-SAPC (Supplementary Fig. 7 and Supplementary Note 5).

Properties of Sb-SAPC and photocatalytic mechanism. The optical properties and the band diagram of Sb-SAPC were investigated. The introduction of Sb and Na species slightly narrowed the bandgap (2.77 eV for PCN and 2.63 eV for Sb-SAPC15), and notably improved the light absorbance (Fig. 1c and Supplementary Fig. 30a,b). Confirmed by valence-band XPS and Mott–Schottky measurements, the introduction of Na and/or Sb species slightly shifted the conduction band minimum from roughly –1.3 eV (versus NHE) to roughly –1.2 eV while rarely influencing the valence band maximum (roughly 1.45 eV) (Supplementary Fig. 30c–g and Supplementary Note 6).

The charge separation and recombination process were monitored by steady-state photoluminescence emission spectroscopy (Supplementary Fig. 31a)⁴³. The radiative recombination of excited charge pairs was clearly observed in pristine PCN while the photoluminescence intensity was markedly reduced with addition of Sb and/or Na, indicating that the radiative recombination was greatly retarded after addition of Sb and/or Na species. This phenomenon is consistent with the highest photocatalytic activity of Sb-SAPC15. In addition, the onset of photoluminescence wavelength gradually red-shifted, which is also consistent with the narrowed bandgap. The facilitated charge migration in Sb-SAPC15 could be further verified by the enhanced photocurrent density (Supplementary Fig. 31c) and decreased electrochemical impedance in the Nyquist plots

(Supplementary Fig. 31b,c). It is noteworthy that the substantially shortened lifetime of photoluminescence (Supplementary Fig. 31d) could be attributed to the generated deeply trapped sites, which have been proved to facilitate the ORR process^{43,44}.

To further investigate whether the deeply trapped sites in Sb-SAPC15 could facilitate both ORR and oxygen evolution reaction (OER), time-resolved-infrared absorption spectroscopy was performed to monitor the charge carrier dynamics and the reactivities of Sb-SAPC15 for ORR and WOR on the microsecond time-scale^{43,45}. To probe the charge-transfer dynamics from electron to O₂ and hole to H₂O, the decay kinetics of deeply trapped electrons (at 5,000 cm^{-1}) of PCN, PCN_Na15 and Sb-SAPC15 were investigated (Supplementary Fig. 32 and Fig. 3a) and compared under N₂, O₂ and H₂O atmospheres (Fig. 3b). The decay of the deeply trapped electrons at 5,000 cm^{-1} on pristine PCN accelerated very slightly (Fig. 3b) in O₂ compared to that in N₂ ($I_{\text{O}_2}/I_{\text{N}_2}=0.83$). The decay on PCN_Na15 showed a little acceleration in O₂ compared to that in N₂ ($I_{\text{O}_2}/I_{\text{N}_2}=0.66$), indicating that introduction of Na could generate reactive sites for charge transfer of trapped electrons to O₂ (refs. 43,44). When Sb was introduced into the catalyst, we observed notable decay of the deeply trapped electrons on Sb-SAPC15 in O₂ as compared to that in N₂ ($I_{\text{O}_2}/I_{\text{N}_2}=0.46$). This indicates that the reactant O₂ would preferentially react with the deeply trapped electrons that were induced by the Sb sites. In the case of holes, the decay on pristine PCN and PCN_Na15 changed very little in H₂O environment compared to that in N₂ ($I_{\text{H}_2\text{O}}/I_{\text{N}_2}=0.86$ for PCN and $I_{\text{H}_2\text{O}}/I_{\text{N}_2}=1.09$ for PCN_Na15), indicating that the photogenerated holes barely transferred to H₂O. On the contrary, the decay on Sb-SAPC15 was substantially retarded in H₂O compared to that in N₂ ($I_{\text{H}_2\text{O}}/I_{\text{N}_2}=1.92$), suggesting that the photogenerated holes could readily transfer to H₂O molecules: hole-consuming reaction by H₂O reduced the number of surviving holes in the catalyst and hence elongated the lifetime of electrons⁴⁵. Additionally, an isotopic experiment (Supplementary Fig. 33) to simulate the real system (without Ag⁺ or NaIO₃) was conducted to verify the as-proposed mechanism of WOR by using ¹⁶O₂ (as an electron acceptor) and H₂¹⁸O (as an electron donor). As shown in Supplementary Fig. 33b, the signal of ¹⁸O₂ (*m/z* = 36) could be detected after photocatalytic reaction for 1 h, indicating that the OER indeed occurred in the real reaction system. It is important to note that this signal could not be detected in absence of Sb-SAPC15 or light irradiation, indicating that the photogenerated holes participated in the WOR to generate ¹⁸O₂. The highly active holes for OER could also be confirmed by rotating ring disc electrode measurements (Supplementary Fig. 34). A clear signal of O₂ reduction to H₂O was detected by the ring disc, verifying O₂ generation on the Sb-SAPC surface via WOR. These results confirm that the deeply trapped electrons and the corresponding holes in Sb-SAPC15 are the major contributors to the ORR and OER processes (Supplementary Note 7), respectively, leading to a notably promoted photocatalytic activity of H₂O₂ production.

The DFT calculation also shows how the Sb and Na species promote the inner and interlayer charge transfer in Sb-SAPC (Supplementary Figs. 35 and 36). Four periodic models including graphitic carbon nitride (GCN), sodium incorporated graphitic carbon nitride (Na-GCN), antimony incorporated graphitic carbon nitride (Sb-GCN) and sodium and antimony co-incorporated graphitic carbon nitride (NaSb-GCN) were optimized, and the Bader charges of each layer in different models are presented in Supplementary Fig. 35 (refs. 43,46). The Bader charge difference between each adjacent layers of pristine GCN is extremely small ($|\Delta q|$ roughly 0.004 e[−]), suggesting very weak adiabatic coupling between interlayers in GCN^{45,46}, leading to poor interlayer charge transfer. Both Na-GCN and Sb-GCN display a relatively large number of electrons accumulating on the second and fourth layer (roughly 0.1 e[−] of layer charge)^{46,47}. As a result, the Na-GCN and Sb-GCN exhibit a high value of charge difference between the adjacent

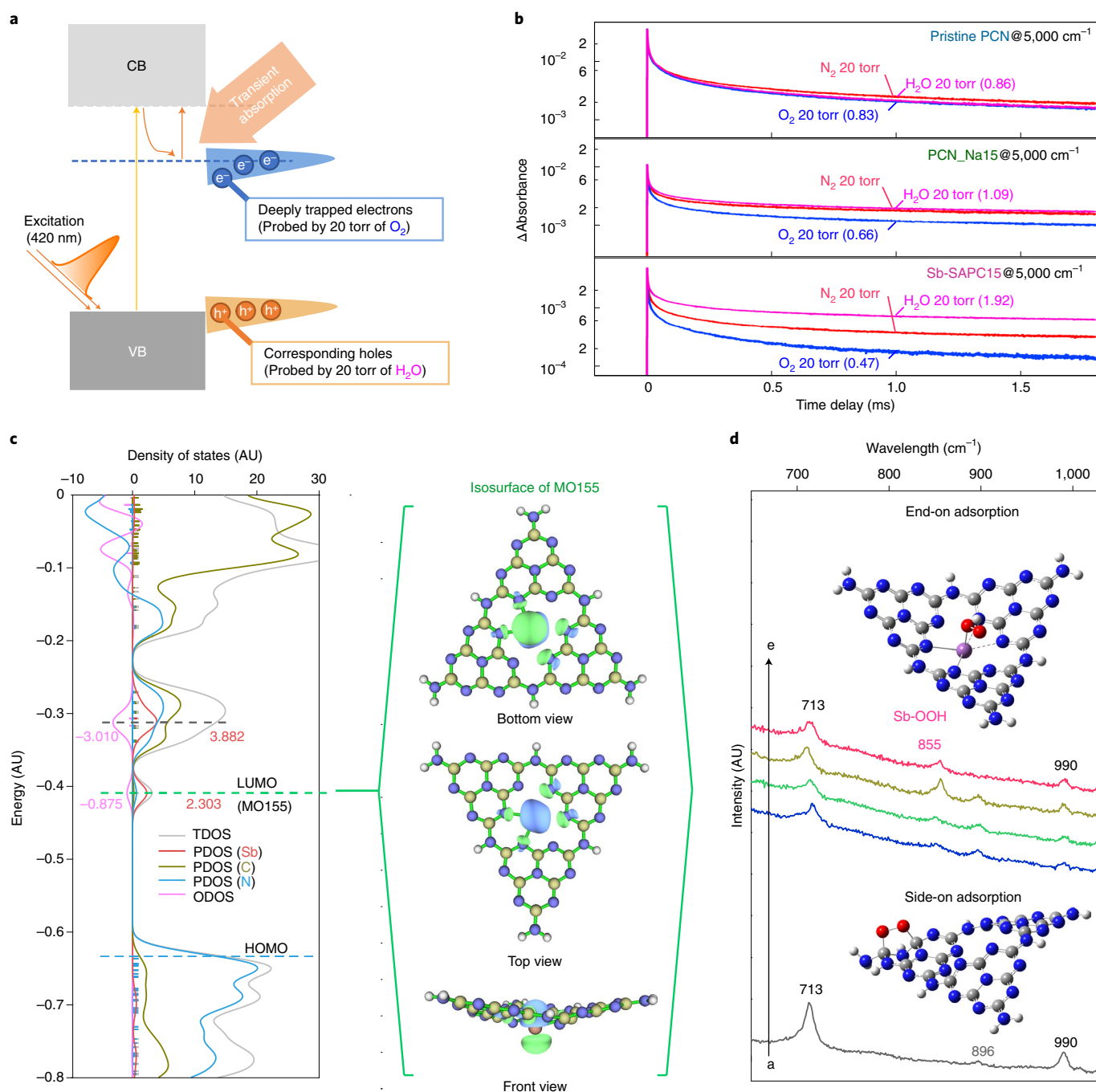


Fig. 3 | Excitation properties and OER/ORR reactivities of Sb-SAPC15. **a**, The systematic diagram of transition absorption after excitation as the probe for OER/ORR (details for the pulse light 420 nm, 6 ns, 5 mJ and 0.2 Hz). **b**, The comparison of transient absorption decay among PCN, PCN_Na15 and Sb-SAPC15 at 5,000 cm^{-1} under N_2 , O_2 and H_2O atmosphere (20 torr). The absorption intensities at the time point of 1 ms was used as the benchmark for investigating how deeply trapped electrons/holes interact with O_2/H_2O . **c**, Total density of states (TDOS), partial density of states (PDOS) and overlapped density of states (ODOS) of Melem_3Sb3+ combined with the isosurface of LUMO (isovalue is 0.05). HOMO, highest occupied molecular orbital. **d**, Experimental Raman spectra recorded during photoreaction in a 2-propanol aqueous solution with saturated oxygen. Spectrum a–d, PCN, Sb-SAPC1, Sb-SAPC5 and Sb-SAPC15 in 10% (v/v) 2-propanol aqueous solution, respectively. Spectrum e, Sb-SAPC15 in pure water. CB and VB indicate the conduction band and valence band, respectively.

layers ($|\Delta q|$ roughly $0.3 e^-$), indicating that adiabatic coupling has been notably boosted by introducing Na or Sb. The copresence of Na and Sb atoms makes the electron distribution more balanced between the layers (Supplementary Fig. 35). In other words, when both Na and Sb are present in the carbon nitride structure, the Na- and Sb-induced electron density polarization can be counterbalanced to

lower the $|\Delta q|$ (roughly $0.05 e^-$) and at the same time the distance for adiabatic coupling is notably increased ($|\Delta q|$ between the first and second layer and between the third and fourth layer are significantly increased). This indicates that the charge transfer between the interlayers in carbon nitride incorporated with Sb and Na atoms is better facilitated than in pristine GCN^{46,47}. The deformation charge density

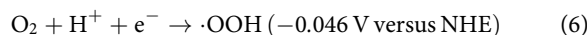
near surface of NaSb-GCN (Supplementary Fig. 36) reveals a clear pathway from Na to Sb. The Sb on the surface of GCN with weak interlayer bridging shows a larger number of electrons accumulating on the first layer ($-0.0395 e^-$ of layer charge) than the second layer ($0.1345 e^-$ of layer charge)^{46–50}. Note that a clear electron accumulation region and an electron depletion region, respectively, are located at the first and second layer while the pristine CN layer (the third layer) can hardly be polarized, indicating that the inner layer charge transfer is substantially improved with incorporation of Sb and Na species^{48–50}. These results show that the electron transfer can be notably promoted by the incorporation of Sb and Na species in GCN, which can explain the higher photocatalytic activities of Sb-SAPC15.

The excited properties of Sb-SAPC were further studied by time-dependent DFT (TDDFT) to understand the correlation between structure and photocatalytic activity using a monolayer cluster model^{51,52}. The possible simulated excited states that contributed to photocatalytic H₂O₂ production (corresponding to the spectra from 420 to 470 nm) were confirmed by comparing the action spectra (Fig. 1c and Supplementary Note 6) with the simulated ones (Supplementary Fig. 37a–c). On the basis of the action spectra and the photocatalytic H₂O₂ production activities, the ES1-16 of Melem_3, the excited states 1–15 of Melem_3Na⁺ and the excited states 1–26 of Melem_3Sb3⁺ are highlighted in the distribution heatmap of photogenerated electrons and holes (Supplementary Fig. 37d–i)⁵³. On the one hand, most of electrons accumulated at the Sb sites (excited states 1–26, Supplementary Table 5), a ligand-to-metal charge transfer from neighbouring melem units to Sb, in Melem_3Sb3⁺ with high density (roughly 20–80%), while most of the states (excited states 1–16 for Melem_3, Supplementary Table 6; excited states 1–15 for Melem_3Na⁺, Supplementary Table 7) show averagely distributed electrons at the C sites (<10%) in Melem_3 and Melem_3Na⁺ (refs. 51–53). Note that the photogenerated electrons and holes barely locate at the Na atoms, indicating that the coordinated Na species on the catalyst's surface could not serve as the active sites for the photocatalytic reaction. Additionally, a comprehensive investigation of charge separation and delocalization of holes and electrons were conducted by using Melem_6, Melem_6Na⁺ and Melem_6Sb3⁺ as models (Supplementary Figs. 38–40 and Supplementary Note 7). The substantially improved separation of electron-hole pairs and highly concentrated electrons/holes may effectively promote both photocatalytic ORR and WOR in Sb-SAPC15 by introducing atomic Sb sites.

The influence of Sb single atoms on the photo-redox reactions was further studied by analysing the contributions of molecular orbital to holes and electrons from ES1 to ES26 of Melem_3Sb3⁺ (Supplementary Table 5). Several molecular orbitals, whose energetic levels are equal to or lower than the highest occupied molecular orbital, all contribute to holes (ranging from 0 to roughly 60%), while almost all electrons are contributed by the lowest occupied molecular orbital (LUMO) (MO155) in most of transitions. This observation indicates that the electronic configuration of LUMO can almost represent the photogenerated electronic configuration. The result from partial DOS (PDOS) of Melem_3Sb3⁺ shows that a new molecular orbital mainly contributed by electrons from Sb forms the LUMO. It is important to note that this molecular orbital exhibits a slightly lower energetic level than the molecular orbital contributed by C and N, which is in accordance with the slightly shifted conduction band minimum of Sb-SAPC15 (ref. 22). Combined with the simulated results of charge separation, isosurface of LUMO of Melem_3Sb3⁺ reveals that most of the electrons (>75%) are concentrated at the single Sb sites with ideal electronic configuration for adsorption of electrophilic oxygen (Fig. 3c). To study the ORR mechanism on Sb-SAPC, rotating disc electrode analysis was performed to investigate the number of electrons (*n*) transferred in the ORR process (Supplementary Fig. 41). The estimated *n* value is close

to 2 for Sb-SAPC15 in both dark and light irradiation conditions. The preferred 2e⁻ ORR pathway on Sb-SAPC can be further supported by DFT calculation using the computational hydrogen electrode method. As shown in Supplementary Fig. 42a, the calculated $\Delta G_{\cdot\text{OOH}}$ is 4.53 eV ($U=0\text{ V}$ versus the reversible hydrogen electrode (RHE)), which is smaller than 4.59 eV of $\Delta G_{\cdot\text{O}}$, a crucial intermediate in 4e⁻ ORR³⁶. The large energetic barrier towards forming *O would suppress the 4e⁻ ORR process. For a 2e⁻ ORR catalyst, the adsorption energy of *OOH should be larger than the thermoneutral value at the equilibrium potential ($U=0.7\text{ V}$ versus RHE), corresponding to $\Delta G_{\cdot\text{OOH}}$ of 3.52 eV. The calculated $\Delta G_{\cdot\text{OOH}}$ is 3.83 eV ($U=0.7\text{ V}$ versus RHE), suggesting that the ORR on single atom Sb may follow a 2e⁻ pathway (Supplementary Fig. 42b). This shows that the difference between *OH and *O is as high as 3.742 eV, indicating that a considerably large energetic barrier needs to be overcome for the 4e⁻ OER process. In this case, the Sb site should not function as an effective site to catalyse 4e⁻ OER. It is noteworthy that the calculated $\Delta G_{\cdot\text{H}}$ on Sb-SAPC15 is substantially larger (0.937 eV) than that on Pt (111) (Supplementary Fig. 43), suggesting that hydrogen evolution reaction on Sb-SAPC15 is energetically unfavourable, matching well with the experimental result (Fig. 1e).

To identify the intermediate in the photocatalytic process, Raman spectroscopy measurements (Fig. 3d) were performed under operando conditions. For PCN, after reaction with 2-propanol as an electron donor under visible light irradiation, a new band appears at 896 cm⁻¹, which can be assigned to the C–O vibration and O–O stretching on the melem¹². While for Sb-SAPCs, a new absorption band at 855 cm⁻¹ increases with Sb content in the sample, which can be assigned to the O–O stretching mode of a Sb-OOH species with end-on adsorption configuration^{54,55}. This relative chemical shift between O₂ end-on/side-on adsorption configuration has been also confirmed by DFT calculations (Supplementary Fig. 44 and Supplementary Note 8). It is noteworthy that Sb-OOH exists even without addition of electron donor, indicating that formation of Sb-OOH, rather than the side-on configuration, dominates in the photocatalytic process on Sb-SAPCs. The end-on adsorption shall notably suppress the 4e⁻ ORR, leading to a high selectivity of the 2e⁻ process^{29,30}. Additionally, electron spin resonance signal of 5,5-dimethyl-1-pyrroline *N*-oxide- $\cdot\text{O}_2^-$ (DMPO- $\cdot\text{O}_2^-$) could be hardly observed in the Sb-SAPC system (Supplementary Fig. 45). Since $\cdot\text{O}_2^-$ is an important intermediate in the stepwise 1e⁻ pathway (equation (6)) during formation of 1–4 endoperoxide, the invisible signal of DMPO- $\cdot\text{O}_2^-$ in the Sb-SAPC system demonstrates rapid reduction of O₂ on Sb-SAPC to generate H₂O₂ via a 2e⁻ ORR pathway^{22,23,55}.



On the basis of the above characterizations and analyses, the reaction mechanism (Fig. 4) of Sb-SAPC for photocatalytic H₂O₂ production is proposed as follows: first, efficient charge separation occurred on Sb-SAPC under visible light irradiation, generating photoexcited electrons and holes for ORR and WOR, respectively. Then, water molecules were oxidized to evolve O₂ by photogenerated holes localized at the N atoms near the single Sb atoms. Simultaneously, O₂ molecules dissolved in water and generated from the WOR both participated in the ORR process to produce H₂O₂. It is worth noting that the efficient charge separation, ideal single atomic sites for end-on type O₂ adsorption and close spatial distribution of active sites boost both the 2e⁻ ORR and 4e⁻ WOR for efficient H₂O₂ production.

Conclusions

In summary, we have reported a well-defined, highly active, selective and photochemically robust single Sb atom photocatalyst for non-sacrificial H₂O₂ production in a water and oxygen mixture

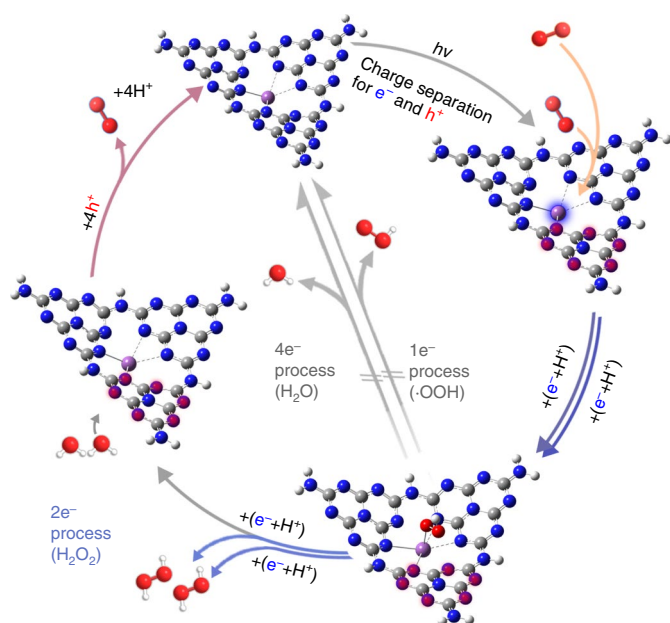


Fig. 4 | Mechanism of photocatalytic H₂O₂ production. The white, grey, blue, red and magenta spheres refer to hydrogen, carbon, nitrogen, oxygen and Sb atoms, respectively. After shining visible light, the photogenerated electrons are localized at the Sb sites (with a blue glow), while the photogenerated holes are localized at the N atoms at the melem units (with a red glow). Subsequently, the dissolved O₂ molecules are adsorbed (orange arrows) onto the Sb sites and then get reduced (blue arrows) via a 2e⁻ transfer pathway through forming an electron μ -peroxide as the intermediate. Simultaneously, water molecules are oxidized (pink arrows) to generate O₂ by the highly concentrated holes on the melem units.

under visible light irradiation. The single Sb sites are able to accumulate electrons, which act as the photoreduction sites for O₂ via a 2e⁻ ORR pathway. Simultaneously, the accumulated holes at the N atoms of the melem units neighbouring to the Sb sites accelerate the water oxidation kinetics. The collaborative effect between the single atom sites and the support shall open up a strategy for designing various SACs for a variety of photocatalytic reactions in energy conversion and environmental remediation.

Methods

Preparation of photocatalysts. Unless otherwise stated, the purities of all reagents for photocatalyst preparation and for photoelectrochemical measurements are above the analytical grade. The pristine PCN and PCN_Na15 were prepared according to the reported methods¹⁹. The Sb-SAPCs were prepared by a bottom-up method as follows: a certain amount of NaSbF₆ (HuNan HuaJing Powdery Material, 0.5 mmol, 1 mmol, 3, 5, 10, 15 and 20 mmol) was dissolved in 30 ml of ethanol under sonication for 60 min at 60 °C, followed by adding 4 g melamine (Wako Pure Chemical Industries). The solvent in the solution was removed by combination of rotatory evaporator and vacuum oven. The obtained white powder was transferred into a tube furnace. To ensure that oxygen was not present during thermal treatment, the tube furnace was first vacuumed to <1 torr before switching on the N₂ gas flow. This process was repeated three times, and then 50 ml min⁻¹ N₂ gas flow was maintained for 30 min before heat treatment. During the synthesis process (including heating and cooling), the system was pressurized by N₂ flow so that oxygen could not influence the synthesis. The temperature of the furnace was increased from 25 °C to 560 °C at a ramp rate of 2 °C min⁻¹ in N₂ atmosphere then kept at 560 °C for 4 h. After heat treatment, the furnace was cooled down naturally to 25 °C lasting for at least 8 h with continuous N₂ flowing.

Photocatalytic reaction towards H₂O₂ production. Here, 100 mg of photocatalyst was added to 50 ml of deionized water in a borosilicate glass bottle (maximum diameter, ϕ 60 mm; capacity 100 ml), and the bottle was sealed with a rubber septum cap. The catalyst was dispersed by ultrasonication for 15 min, and O₂ was bubbled through the solution for 30 min. The bottle was kept in a temperature-controlled air bath at 25 ± 0.5 °C with wind flow and was irradiated

at $\lambda > 420$ nm using a 300 W Xe lamp (PXE-500, USHIO Inc.) under magnetic stirring. To study the WOR, 50 mg of photocatalyst was added into NaIO₃ (0.1 M, 50 ml) solution in a borosilicate glass bottle (ϕ 60 mm; capacity 100 ml). After completely removing O₂ from the reaction system, the bottle was irradiated by a 300 W Xenon Lamp. The light intensity of visible light and infrared light ($I_{>400}$) after passing an ultraviolet (UV) cut filter ($\lambda > 400$ nm) was first measured. Then, a glass filter with $\lambda > 500$ nm was used to replace the UV cut filter for measuring the light intensity ($I_{>500}$). The difference between $I_{>400}$ and $I_{>500}$ was used to calibrate the total light intensity. After a certain time interval, the gas was extracted from the bottle and examined by gas chromatography equipped with a thermal conductivity detector. To examine the H₂O₂ production from O₂ generated by WOR, a certain amount of photocatalyst (Sb-SAPC15 200, 100 and 50 mg; Pristine PCN 200 mg) was added into 50 ml of NaNO₃ solution (pH 7) with AgNO₃ (0.1 mM). Every hour, 1.5 ml of solution was extracted to acquire the time-dependent H₂O₂ production without the initial introduction of O₂. The amount of H₂O₂ in these experiments was determined by a colorimetric method using PACKTEST (WAK-H₂O₂, Kyoritsu Chemical-Check Laboratory, Corp.) equipped with a digital PACKTEST spectrometer (ED723, GL Sciences Inc.).

Apparent quantum efficiency analysis. The photocatalytic reaction was carried out in pure deionized water (30 ml) with photocatalyst (60 mg) and with or without addition of ethanol as an electron donor in a borosilicate glass bottle. After ultrasonication and O₂ bubbling, the bottle was irradiated by an Xe lamp for 4 h with magnetic stirring. The incident light was monochromated by band-pass glass filters (Asahi Techno Glass Co.), where the full-width at half-maximum of the light was 11–16 nm. The number of photons that enter the reaction vessel was determined by a 3684 optical power meter (Hioki E.E. Corp.).

Determination of solar-to-chemical conversion efficiency. Solar-to-chemical conversion efficiency was determined by a PEC-L01 solar simulator (Pecell Technologies, Inc.). The photoreaction was performed in pure deionized water (100 ml) with photocatalyst (500 mg) under an O₂ atmosphere (1 atm) in a borosilicate glass bottle. A UV cut filter ($\lambda > 420$ nm) was used to avoid decomposition of the formed H₂O₂ by absorbing UV light^{12,16,23}. The irradiance of the solar simulator was adjusted to the AM1.5 global spectrum^{12,16,23}. The solar-to-chemical conversion efficiency (η) was calculated by equation (7):

$$\eta (\%) = \frac{\Delta G_{\text{H}_2\text{O}_2} \times n_{\text{H}_2\text{O}_2}}{t_{\text{ir}} \times S_{\text{ir}} \times I_{\text{AM}}} \times 100\%. \quad (7)$$

where $\Delta G_{\text{H}_2\text{O}_2}$ is the free energy for H₂O₂ generation (117 kJ mol⁻¹), $n_{\text{H}_2\text{O}_2}$ is the amount of H₂O₂ generated and t_{ir} is the irradiation time (s). The overall irradiation intensity (I_{AM}) of the AM1.5 global spectrum (300–2,500 nm) is 1,000 W m⁻² and the irradiation area (S_{ir}) is 3.14×10^{-4} m².

Instruments. HRTEM, HAADF-STEM, selected area electron diffraction and energy-dispersive X-ray spectroscopy were performed on a Titan Cubed Themis G2 300 electron microscope with an accelerating voltage of 300 kV. EELS was conducted using a Quantum ER/965 P detector. The crystalline phases were characterized by a powder X-ray diffraction instrument (MiniFlex II, Rigaku) with CuK α ($\lambda = 1.5418$ Å) radiation (cathode voltage 30 kV, current 15 mA). Absorption properties of the powder samples were determined using the diffuse reflection method on a UV-visible light near-infrared spectrometer (UV-2600, Shimadzu) attached to an integral sphere at room temperature. XPS measurements were performed on a Kratos AXIS Nova spectrometer (Shimadzu) with a monochromatic Al K α X-ray source. The binding energy was calibrated by taking the carbon (C) 1s peak of adventitious carbon at 284.6 eV. Valence-band XPS was performed on an ESCALAB 250Xi (Thermo Scientific). The equilibration of Fermi level of the instrument was performed by measuring the VB-XPS of Au metal basis as the reference. The Fermi level of the instrument was equilibrated at 4.5 eV. In this case, the numerical value of the binding energy in the calibrated VB-XPS spectrum is the same as the potential versus standard hydrogen electrode. Electron spin resonance signals of spin-trapped paramagnetic species with 5,5-dimethyl-1-pyrroline N-oxide (DMPO, methanol solution) were recorded with an A300-10/12 spectrometer. Photoluminescence spectroscopy was performed on a FP-8500 spectrofluorometer (JASCO Corporation). The temperature for the photoluminescence measurements was about 25 °C controlled by an air conditioner, which worked 24/7. Time-dependent photoluminescence spectroscopy was conducted on a FS5 fluorescence spectrometer (Edinburgh Instruments). Raman spectroscopy was performed on a Laser Microscopic Confocal Raman Spectrometer (Renishaw in Via) at 785 nm. The pH value of the solution was measured by a pH meter (HORIBA pH meter D-51, Horiba).

The X-ray absorption spectroscopy for the Sb K-edge was measured at beamline BL01C at the National Synchrotron Radiation Research Center (NSRRRC, Hsinchu, Taiwan). The data analysis for the X-ray absorption spectroscopy using IFEFFIT was conducted using the Demeter system.

Photoelectrochemical characterizations. Photoelectrochemical characterizations were conducted on a conventional three-electrode potentiostat setup connected to an electrochemical analyser (Model 604D, CH Instruments). The fluorine-doped

tin oxide (FTO) glass of 1 × 2 cm in size was covered with photocatalyst that was achieved by first mixing a catalyst (100 mg) with ethyl cellulose binder (10 mg) in ethanol (6 ml) for 1 h and then depositing the final viscous mixture by a doctor blade method, followed by drying at room temperature and further drying at 40 °C overnight in a vacuum oven. The area of the photoelectrode was controlled to be 1 cm². The photoelectrochemical system consisted of an FTO glass covered by the photocatalyst, a coiled Pt wire and a saturated Ag/AgCl/KCl (saturated) electrode as the working, counter and reference electrode, respectively. The photocurrent was collected at 0.8 V versus NHE (0.6 V versus Ag/AgCl) in a phosphate buffer solution (PBS, pH 7.4). The solution was saturated with O₂ by bubbling O₂ for 15 min (0.51 min⁻¹)^{12,56,57}. Electrochemical impedance spectroscopy analysis was performed at a d.c. voltage of -0.6 V versus Ag/AgCl with an a.c. voltage amplitude of 5 mV in a frequency range from 100 kHz to 0.01 Hz. For the Mott–Schottky measurements, similar strategy was performed on FTO glass (1.5 × 3 cm) by the same doctor blade method. The area of the electrode for the Mott–Schottky measurements was controlled to be 0.50 cm². Mott–Schottky measurements were performed at a potential range from 0.2 V to -0.6 V versus NHE, with an a.c. voltage amplitude of 5 mV and in a frequency range of 25–500 Hz. Each increase of potential is 0.05 V. The quiet time for each test is 2 s.

Isotopic experiments with ¹⁸O₂ and H₂¹⁶O. First, 60 mg of Sb-SAPC15 was dispersed in 30 ml of H₂¹⁶O via sonication for 15 min. Subsequently, 10 ml of ¹⁸O₂ gas (≥98% ¹⁸O; Taiyo Nippon Sanso Corporation) was injected to the suspension. Then, the system was completely sealed and irradiated by visible light. After a certain time interval (6, 24 and 72 h), 1 ml of suspension was extracted and injected into a glass test tube filled with N₂ and 0.1 g of Fe₂(SO₄)₃ dissolved in 1 ml of H₂SO₄. After injection of suspension, the test tube was sealed and irradiated under UV light for 5 h. The gas (0.1 ml) in the test tube was extracted by gas chromatography syringe and injected into a Shimadzu GC–MS system (GC–MS–QP2010).

Isotopic experiments with H₂¹⁸O. Here, 20 mg of Sb-SAPC15 was dispersed in 10 g of H₂¹⁸O (≥98% ¹⁸O; Taiyo Nippon Sanso Corporation) containing 1 mM AgNO₃ under sonication for 15 min. Afterwards, N₂ was bubbled into the suspension for 2 h at a flow rate of 0.51 min⁻¹ to ensure complete removal of the dissolved oxygen (¹⁶O₂) in the system¹⁶. Then, the system was completely sealed and irradiated by visible light. After a certain time interval (0.5, 1, 3, 5, 10 and 24 h), 1 ml of suspension was extracted and injected into a glass test tube filled with N₂ and 0.1 g Fe₂(SO₄)₃ dissolved in 1 ml of H₂SO₄. After injection of suspension, the test tube was sealed and irradiated under UV light for 5 h. The gas (0.1 ml) in the test tube was extracted by gas chromatography syringe and injected into a Shimadzu GC–MS system (GC–MS–QP2010).

Isotopic experiments in real experimental conditions. A poly-tetrafluoroethylene gas bag was used for the isotopic experiment. First of all, 3 ml ultrapure N₂ was injected into the bag, followed by injecting 1 ml aqueous suspension of Sb-SAPC15 (concentration 1 mg ml⁻¹; 1 mg of Sb-SAPC15 powder dissolved in 1 ml of H₂¹⁸O). Subsequently, 100 μl of O₂ gas was injected and the bag was properly sealed and put over an ultrasonicator. Additionally, control experiments in absence of Sb-SAPC15 or light irradiation were conducted for confirming the photo-induced oxygen generation reaction. Furthermore, GC–MS spectra of the gas extracted from the Sb-SAPC15 system with other electron acceptors (0.1 M Ag⁺ or 0.1 M NaIO₃) or without addition of Sb-SAPC were also conducted for comparison.

H₂O₂ degradation study. Here, 50 ml of deionized water in a borosilicate glass bottle (φ 60 mm; capacity 100 ml) without addition of catalyst was bubbled with O₂ for 30 min. Then, a certain amount of H₂O₂ was added into the bottle, and the concentration of H₂O₂ was manipulated to be 1 × 10² mg l⁻¹. Finally, the bottle was sealed with a rubber septum cap. To investigate the hole transfer to H₂O₂, the following experiment was performed: 50 mg of photocatalyst was added into 50 ml of NaIO₃ (0.1 M) and H₂O₂ (0.01 wt%) solution in a borosilicate glass bottle (φ 60 mm; capacity 100 ml). The same solution without addition of photocatalyst was also measured as a control. Additionally, the same experiment was also conducted in 50 ml of NaIO₃ (0.1 M) phosphate buffer solution (0.1 M, pH 7.4). After completely removing O₂ from the reaction system, the bottle was irradiated by a 300 W Xenon lamp with a UV cut filter (light intensity 30.3 W m⁻² at 420–500 nm).

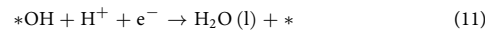
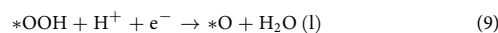
Details for TDDFT calculations. The optimization and frequency combined with vertical excitation properties were performed via TDDFT in the Gaussian 09 program S2, which was carried out by using the wb97xd/6-311g(d) level of theory for C, N and H elements and SDD for Sb element. Three monolayer cluster models were optimized to represent the major surface properties of CN sites in PCN, Na sites in PCN_Na15 and Sb sites in Sb-SAPC15 (refs. ^{50,58}). The charges of monolayer cluster models were settled in consideration of the oxidation state of Sb and Na on the basis of the experimental results as follows: 0 for Melem_3; +1 for Melem_Na1⁺ and +3 for Melem_3Sb3⁺. To give a comprehensive understanding of the relationships between the electronic configuration during excitation and the realistic experiment results, 50 excited states of these three cluster models were used to simulate UV absorption spectra⁴⁰. Note that the absorption edges of simulated UV spectra are unusually large compared to those of experimental ones

for two reasons: (1) to simulate the charge-transfer properties of the high-quality model, functions of ω 97xd, a function including a large amount of Hartree–Fock exchange, were used. These exchange functions usually overestimate the excitation energies, as well as the simulated highest to lowest highest occupied molecular orbital gap^{51,52,58}. (2) In the solid state, p-conjugated molecules adjacent to the one carrying a charge become strongly polarized, an effect that stabilizes the cationic and anionic states (each generally by about one eV in p-conjugated materials). In this case, the bandgap is typically considerably lower in energy than the molecular fundamental gap and the optical gap⁵². Since the evitable system error cannot be eliminated, the possible simulated excited states that contributed to H₂O₂ production (corresponding to spectra from 420–470 nm) were confirmed by comparing the experimental spectra and simulated ones. Then, the transition density of electron/holes were considered at all these excited states.

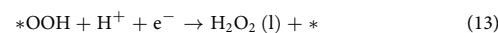
For analysis of the excitation and charge-transfer properties, Multiwfn v.3.6 (released on 21 May 2019)⁵³ was performed. Visualization of hole, electron and transition density was also performed by Multiwfn; functions of IOP(9/40=3) were set during the vertical excitation based on TDDFT calculation⁵³. The electron distributions at these excited states were presented as heatmaps by combination of GaussView and Multiwfn^{53,59–62}. The isosurface of LUMO orbitals were presented by setting the isovalue at 0.05.

Details for the free energy diagram. The cluster model is more likely to predict the ORR process on the basis of our previous investigation³⁶. The free energy diagram of Melem_3Sb3⁺ was calculated as follows:

The optimized structure of Melem_3Sb3⁺ was used as the initial structure for calculating the most stable adsorption configurations of *OOH, *O and *OH. The ORR following the 2e⁻ and 4e⁻ pathway produces H₂O and H₂O₂, respectively. The associative 4e⁻ ORR is composed of four elementary steps (equations (8)–(11)):



The 2e⁻ ORR comprises two elementary steps (equations (12) and (13)):



The asterisk (*) denotes the active site of the catalyst.

The free energy for each reaction intermediate is defined as:

$$G = E_{\text{DFT}} + E_{\text{ZPE}} - T_{\text{s}} + E_{\text{sol}} \quad (14)$$

where E_{DFT} is the electronic energy calculated by DFT, E_{ZPE} denotes the zero point energy estimated within the harmonic approximation and T_{s} is the entropy at 298.15 K ($T = 298.15$ K). The E_{ZPE} and T_{s} of gas-phase H₂ and reaction intermediates are based on our previous work³⁶. For the concerted proton–electron transfer, the free energy of a pair of proton and electron (H⁺ + e⁻) was calculated as a function of applied potential relative to RHE (U versus RHE), that is, $\mu(\text{H}^+) + \mu(\text{e}^-) = 1/2\mu(\text{H}_2) - eU$, according to the computational hydrogen electrode model proposed by Nørskov⁶³. In addition, the solvent effect was reported to play an important role in ORR. In our calculations, the solvent corrections (E_{sol}) for *OOH and *OH are 0.45 eV in accordance with previous studies^{64,65}. We used the energies of H₂O and H₂ molecules calculated by DFT together with experimental formation energy of H₂O (4.92 eV) to construct the free energy diagram. The free energies of O₂, *OOH, *O and *OH at a given potential U relative to RHE are defined as:

$$\Delta G(\text{O}_2) = 4.92 - 4eU \quad (15)$$

$$\Delta G(\text{OOH}) = G(*\text{OOH}) + \frac{3G(\text{H}_2)}{2} - G(*) - 2G(\text{H}_2\text{O}) - 3eU \quad (16)$$

$$\Delta G(\text{O}) = G(*\text{O}) + G(\text{H}_2) - G(*) - G(\text{H}_2\text{O}) - 2eU \quad (17)$$

$$\Delta G(\text{OH}) = G(*\text{OH}) + \frac{G(\text{H}_2)}{2} - G(*) - G(\text{H}_2\text{O}) - eU \quad (18)$$

Details for simulations of charge transfer. All theoretical calculations were performed based on DFT, implemented in the Vienna ab initio simulation package^{66,67}. The electron exchange and correlation energy were treated within the generalized gradient approximation in the Perdew–Burke–Ernzerhof

functional^{68,69}. The valence orbitals were described by plane-wave basis sets with cutoff energies of 400 eV. For the simulation of Na and Sb incorporated in bulk phase of g-C₃N₄, a 1 × 1 × 2 supercell of pristine bulk g-C₃N₄ was adopted. And the *k*-points were sampled in a 3 × 3 × 2 Monkhorst–Pack grid. For the simulation of Na and Sb near the surface of g-C₃N₄, the *k*-point sampling was obtained from the Monkhorst–Pack scheme with a (2 × 2 × 1) mesh. The atomic coordinates are fully relaxed using the conjugate gradient method⁷⁰. The convergence criteria for the electronic self-consistent iteration and force were set to 10⁻⁴ eV and 0.02 eV Å⁻¹, respectively. The vacuum gap was set as 15 Å. To quantitatively compare the degree of charge transfer, a Bader charge analysis has been carried out⁶⁵.

Data availability

Source data are provided with this paper. The data that support the findings of this study are available from the corresponding author upon reasonable request.

Received: 7 June 2020; Accepted: 16 March 2021;

Published online: 21 May 2021

References

- Bryliakov, K. P. Catalytic asymmetric oxygenations with the environmentally benign oxidants H₂O₂ and O₂. *Chem. Rev.* **117**, 11406–11459 (2017).
- Shaegh, S. A. M., Nguyen, N.-T., Ehteshamiab, S. M. M. & Chan, S. H. A membraneless hydrogen peroxide fuel cell using Prussian Blue as cathode material. *Energy Environ. Sci.* **5**, 8225–8228 (2012).
- Gray, H. B. Powering the planet with solar fuel. *Nat. Chem.* **1**, 7 (2009).
- Kim, D., Sakimoto, K. K., Hong, D. & Yang, P. Artificial photosynthesis for sustainable fuel and chemical production. *Angew. Chem. Int. Ed.* **54**, 3259–3266 (2015).
- Xia, C., Xia, Y., Zhu, P., Fan, L. & Wang, H. Direct electrosynthesis of pure aqueous H₂O₂ solutions up to 20% by weight using a solid electrolyte. *Science* **366**, 226–231 (2019).
- Edwards, J. K. et al. Direct synthesis of H₂O₂ from H₂ and O₂ over gold, palladium, and gold-palladium catalysts supported on acid-pretreated TiO₂. *Angew. Chem. Int. Ed.* **48**, 8512–8515 (2009).
- Freakley, S. J. et al. Palladium-tin catalysts for the direct synthesis of H₂O₂ with high selectivity. *Science* **351**, 965–968 (2016).
- Yang, S. et al. Toward the decentralized electrochemical production of H₂O₂: a focus on the catalysis. *ACS Catal.* **8**, 4064–4081 (2018).
- Yi, Y., Wang, L., Li, G. & Guo, H. A review on research progress in the direct synthesis of hydrogen peroxide from hydrogen and oxygen: noble-metal catalytic method, fuel-cell method and plasma method. *Catal. Sci. Technol.* **6**, 1593–1610 (2016).
- Hou, H., Zeng, X. & Zhang, X. Production of hydrogen peroxide through photocatalytic process. *Angew. Chem. Int. Ed.* **59**, 17356–17376 (2020).
- Shi, X. et al. Understanding activity trends in electrochemical water oxidation to form hydrogen peroxide. *Nat. Commun.* **8**, 701 (2017).
- Shiraishi, Y. et al. Sunlight-driven hydrogen peroxide production from water and molecular oxygen by metal-free photocatalysts. *Angew. Chem.* **126**, 13672–13677 (2014).
- Fuku, K. & Sayama, K. Efficient oxidative hydrogen peroxide production and accumulation in photoelectrochemical water splitting using a tungsten trioxide/bismuth vanadate photoanode. *Chem. Commun.* **52**, 5406–5409 (2016).
- Baek, J. H. et al. Selective and efficient Gd-doped BiVO₄ photoanode for two-electron water oxidation to H₂O₂. *ACS Energy Lett.* **4**, 720–728 (2019).
- Teng, Z. et al. Photoexcited single metal atom catalysts for heterogeneous photocatalytic H₂O₂ production: pragmatic guidelines for predicting charge separation. *Appl. Catal. B Environ.* **282**, 119589 (2020).
- Shiraishi, Y. et al. Resorcinol–formaldehyde resins as metal-free semiconductor photocatalysts for solar-to-hydrogen peroxide energy conversion. *Nat. Mater.* **18**, 985–993 (2019).
- Fan, W. et al. Efficient hydrogen peroxide synthesis by metal-free polyterthiophene via photoelectrocatalytic dioxygen reduction. *Energy Environ. Sci.* **13**, 238–245 (2020).
- Kim, H., Choi, Y., Hu, S., Choi, W. & Kim, J.-H. Photocatalytic hydrogen peroxide production by anthraquinone-augmented polymeric carbon nitride. *Appl. Catal. B Environ.* **229**, 121–129 (2018).
- Moon, G.-H. et al. Eco-friendly photochemical production of H₂O₂ through O₂ reduction over carbon nitride frameworks incorporated with multiple heteroelements. *ACS Catal.* **7**, 2886–2895 (2017).
- Chu, C. et al. Spatially separating redox centers on 2D carbon nitride with cobalt single atom for photocatalytic H₂O₂ production. *Proc. Natl Acad. Sci. USA* **117**, 6376–6382 (2020).
- Wei, Z. et al. Efficient visible-light-driven selective oxygen reduction to hydrogen peroxide by oxygen-enriched graphitic carbon nitride polymer. *Energy Environ. Sci.* **11**, 2581–2589 (2018).
- Kaynan, N., Berke, B. A., Hazut, O. & Yerushalmi, R. Sustainable photocatalytic production of hydrogen peroxide from water and molecular oxygen. *J. Mater. Chem. A* **2**, 13822–13826 (2014).
- Teng, Z. et al. Bandgap engineering of polymetric carbon nitride copolymerized by 2,5,8-triamino-tri-s-triazine (melem) and barbituric acid for efficient nonsacrificial photocatalytic H₂O₂ production. *Appl. Catal. B.* **271**, 118917 (2020).
- Zeng, X. et al. Simultaneously tuning charge separation and oxygen reduction pathway on graphitic carbon nitride by polyethylenimine for boosted photocatalytic hydrogen peroxide production. *ACS Catal.* **10**, 3697–3706 (2020).
- Wang, Q. & Domen, K. Particulate photocatalysts for light-driven water splitting: mechanisms, challenges, and design strategies. *Chem. Rev.* **120**, 919–985 (2020).
- Hirakawa, H., Hashimoto, M., Shiraishi, Y. & Hirai, T. Photocatalytic conversion of nitrogen to ammonia with water on surface oxygen vacancies of titanium dioxide photocatalytic conversion of nitrogen to ammonia with water on surface oxygen vacancies of titanium dioxide. *J. Am. Chem. Soc.* **139**, 10929–10936 (2017).
- Kulkarni, A., Siahrostami, S., Patel, A. & Nørskov, J. K. Understanding catalytic activity trends in the oxygen reduction reaction. *Chem. Rev.* **118**, 2302–2312 (2018).
- Watanabe, E., Ushiyama, H. & Yamashita, K. Theoretical studies on the mechanism of oxygen reduction reaction on clean and O-substituted Ta₃N₅(100) surfaces. *Catal. Sci. Technol.* **5**, 2769–2776 (2015).
- Choi, C. H. et al. Hydrogen peroxide synthesis via enhanced two-electron oxygen reduction pathway on carbon-coated Pt surface. *J. Phys. Chem. C* **118**, 30063–30070 (2014).
- Chu, C. et al. Electronic tuning of metal nanoparticles for highly efficient photocatalytic hydrogen peroxide production. *ACS Catal.* **9**, 626–631 (2019).
- Pegis, M. L., Wise, C. F., Martin, D. J. & Mayer, J. M. Oxygen reduction by homogeneous molecular catalysts and electrocatalysts. *Chem. Rev.* **118**, 2340–2391 (2018).
- Yang, S., Kim, J., Tak, Y. J., Soon, A. & Lee, H. Single-atom catalyst of platinum supported on titanium nitride for selective electrochemical reactions. *Angew. Chem. Int. Ed.* **55**, 2058–2062 (2016).
- Montemore, M. M., van Spronsen, M. A., Madix, R. J. & Friend, C. M. O₂ activation by metal surfaces: implications for bonding and reactivity on heterogeneous catalysts. *Chem. Rev.* **118**, 2816–2862 (2018).
- Wang, A., Li, J. & Zhang, T. Heterogeneous single-atom catalysis. *Nat. Rev. Chem.* **2**, 65–81 (2018).
- Shen, R. et al. High-concentration single atomic Pt sites on hollow Cu₂S for selective O₂ reduction to H₂O₂ in acid solution. *Chem* **5**, 2099–2110 (2019).
- Gao, J. et al. Enabling direct H₂O₂ production in acidic media through rational design of transition metal single atom catalyst. *Chem* **6**, 1–17 (2020).
- Jung, E. et al. Atomic-level tuning of Co-C-N catalyst for high performance electrochemical H₂O₂ production. *Nat. Mater.* **19**, 436–442 (2020).
- Nosaka, Y. & Nosaka, A. *Introduction to Photocatalysis: From Basic Science to Applications* (Royal Society of Chemistry, 2016).
- Inoue, Y. Photocatalytic water splitting by RuO₂-loaded metal oxides and nitrides with d⁸- and d¹⁰-related electronic configurations. *Energy Environ. Sci.* **2**, 364–386 (2009).
- Li, X. et al. Single-atom Pt as co-catalyst for enhanced photocatalytic H₂ evolution. *Adv. Mater.* **28**, 2427–2431 (2016).
- Naumkin, A. V., Kraut-Vass, A., Gaarenstroom, S. W. & Powell, C. J. *NIST X-Ray Photoelectron Spectroscopy Database* figshare (NIST, 2012); <https://doi.org/10.18434/T4T88K>
- Ravel, B. & Newville, M. ATHENA, ARTEMIS, HEPHAESTUS: data analysis for X-ray absorption spectroscopy using IFEFFIT. *J. Synchrotron Radiat.* **12**, 537–541 (2005).
- Zhang, P. et al. Heteroatom dopants promote two-electron O₂ reduction for photocatalytic production of H₂O₂ on polymeric carbon nitride. *Angew. Chem. Int. Ed.* **59**, 16209–16217 (2020).
- Kim, S. et al. Selective charge transfer to dioxygen on KPF₆-modified carbon nitride for photocatalytic synthesis of H₂O₂ under visible light. *J. Catal.* **357**, 51–58 (2018).
- Yamakata, A., Ishibashi, T. & Onishi, H. Water- and oxygen-induced decay kinetics of photogenerated electrons in TiO₂ and Pt/TiO₂: a time-resolved infrared absorption study. *J. Phys. Chem. B* **105**, 7258–7262 (2001).
- Zhang, P. et al. Modified carbon nitride nanzyme as bifunctional glucose oxidase-peroxidase for metal-free bioinspired cascade photocatalysis. *Nat. Commun.* **10**, 940 (2019).
- Sanville, E., Kenny, S. D., Smith, R. & Henkelman, G. Improved grid based algorithm for Bader charge allocation. *J. Comput. Chem.* **28**, 899–908 (2001).
- Gao, H., Yan, S., Wang, J. & Zou, Z. Ion coordination significantly enhances the photocatalytic activity of graphitic-phase carbon nitride. *Dalton Trans.* **43**, 8178–8183 (2014).
- Xiong, T. et al. KCl-mediated dual electronic channels in layered g-C₃N₄ for enhanced visible light photocatalytic NO removal. *Nanoscale* **10**, 8066–8074 (2018).
- Xiong, T., Cen, W., Zhang, Y. & Dong, F. Bridging the g-C₃N₄ interlayers for enhanced photocatalysis. *ACS Catal.* **6**, 2462–2472 (2016).

51. Ghuman, K. K. et al. Photoexcited surface frustrated Lewis pairs for heterogeneous photocatalytic CO₂ reduction. *J. Am. Chem. Soc.* **138**, 1206–1214 (2016).
52. Bredas, J.-L. Mind the gap! *Mater. Horiz.* **1**, 17–19 (2014).
53. Lu, T. & Chen, F. Multiwfn: A multifunctional wavefunction analyzer. *J. Comput. Chem.* **33**, 580–592 (2012).
54. Nakamura, R. & Nakato, Y. Primary intermediates of oxygen photoevolution reaction on TiO₂ (rutile) particles, revealed by in situ FTIR absorption and photoluminescence measurements. *J. Am. Chem. Soc.* **126**, 1290–1298 (2004).
55. Jones, R., Summerville, D. & Basolo, F. Synthetic oxygen carriers related to biological systems. *Chem. Rev.* **79**, 139–179 (1979).
56. Li, S. et al. Effective photocatalytic H₂O₂ production under visible light irradiation at g-C₃N₄ modulated by carbon vacancies. *Appl. Catal. B* **190**, 26–35 (2016).
57. Kofuji, Y. et al. Carbon nitride–aromatic diimide–graphene nanohybrids: metal-free photocatalysts for solar-to-hydrogen peroxide energy conversion with 0.2% efficiency. *J. Am. Chem. Soc.* **138**, 10019–10025 (2016).
58. Govind, N., Lopata, K., Rousseau, R., Andersen, A. & Kowalski, K. Visible light absorption of N-doped TiO₂ rutile using (LR/RT)-TDDFT and active space EOMCCSD calculations. *J. Phys. Chem. Lett.* **2**, 2696–2701 (2011).
59. Bahers, T. L., Adamo, C. & Ciofini, I. A qualitative index of spatial extent in charge-transfer excitations. *J. Chem. Theory Comput.* **7**, 2498–2506 (2011).
60. Kraner, S., Scholz, R., Plasser, F., Koerner, C. & Leo, K. Exciton size and binding energy limitations in one-dimensional organic materials. *J. Chem. Phys.* **143**, 244905 (2015).
61. Kraner, S., Prampolini, O. & Cuniberti, G. Exciton binding energy in molecular triads. *J. Phys. Chem. C* **121**, 17088–17095 (2017).
62. Kislitsyn, D. et al. Spatial mapping of sub-bandgap states induced by local nonstoichiometry in individual lead sulfide nanocrystals. *J. Phys. Chem. Lett.* **5**, 3701–3707 (2014).
63. Nørskov, J. K. et al. Origin of the overpotential for oxygen reduction at a fuel-cell cathode. *J. Phys. Chem. B* **108**, 17886–17892 (2004).
64. Calle-Vallejo, F., Martí'nez, J. I. & Rossmeisl, J. Density functional studies of functionalized graphitic materials with late transition metals for oxygen reduction reactions. *Phys. Chem. Chem. Phys.* **13**, 15639–15643 (2011).
65. Xu, H., Cheng, D., Cao, D. & Zeng, X. C. A universal principle for a rational design of single-atom electrocatalysts. *Nat. Catal.* **1**, 339–348 (2018).
66. Kresse, G. & Furthmüller, J. Efficient iterative schemes for ab initio total-energy calculations using a plane-wave basis set. *J. Phys. Rev. B* **54**, 11169–11186 (1996).
67. Kresse, G. & Furthmüller, J. Efficiency of ab-initio total energy calculations for metals and semiconductors using a plane-wave basis set. *J. Comput. Mater. Sci.* **6**, 15–50 (1996).
68. Perdew, J. P., Burke, K. & Ernzerhof, M. Generalized gradient approximation made simple. *Phys. Rev. Lett.* **77**, 3865–3868 (1996).
69. Blöchl, P. E. Projector augmented-wave method. *Phys. Rev. B* **50**, 17953–17979 (1994).
70. Press, W. H., Teukolsky, S. A., Vetterling, W. T. & Flannery, B. P. *Numerical Recipes* (Cambridge Univ. Press, 2007).

Acknowledgements

We acknowledge the financial support from the Mitsubishi Chemical Corporation, Japan Society for the Promotion of Science (JSPS) Grant-in-Aid for Scientific Research (B, grant no. 20H02847), Grant-in-Aid for JSPS Fellows (DC2, grant no. 20J13064), Project National Natural Science Foundation of China (grant nos. 21805191, 21972094), the Guangdong Basic and Applied Basic Research Foundation (grant no. 2020A1515010982), Shenzhen Pengcheng Scholar Program, Shenzhen Peacock Plan (grant nos. KQJSCX20170727100802505 and KQTD2016053112042971), the Singapore Ministry of Education (Tier 1: RG4/20 and Tier 2: MOET2EP10120-0002) and the Agency for Science, Technology and Research (A*Star IRG: A20E5c0080). We thank X. Huang from the Department of Physics, Southern University of Science and Technology for his help in theoretical calculation and N. Jian from the Electron Microscope Center of the Shenzhen University for his help in HRTEM measurement.

Author contributions

Z.T., Q.Z. and T.O. conceptualized the project. T.O., C.S. and B.L. supervised the project. Z.T. synthesized the catalysts, conducted the catalytic tests and the related data processing, and performed materials characterization and analysis with the help of H.Y., Q.Z., Y.-R.L. and S.L. K.K. and A.Y. conducted transient absorption spectroscopy. Z.T., W.Y. and C.W. performed the theoretical study. Z.T., H.Y. and B.L. wrote the paper with support from all authors.

Competing interests

The authors declare no competing interests.

Additional information

Supplementary information The online version contains supplementary material available at <https://doi.org/10.1038/s41929-021-00605-1>.

Correspondence and requests for materials should be addressed to C.S., B.L. or T.O.

Peer review information *Nature Catalysis* thanks Wei Lin and the other, anonymous, reviewer(s) for their contribution to the peer review of this work.

Reprints and permissions information is available at www.nature.com/reprints.

Publisher's note Springer Nature remains neutral with regard to jurisdictional claims in published maps and institutional affiliations.

© The Author(s), under exclusive licence to Springer Nature Limited 2021, corrected publication 2021